



Study on SWCC and PSD evolution of compacted loess before and after drying-wetting cycles

Haiman Wang^{1,2} · Wankui Ni^{1,2} · Kangze Yuan^{1,2} · Yongpeng Nie^{1,2} · Lan Li^{1,3}

Received: 16 December 2020 / Accepted: 10 April 2023 / Published online: 20 April 2023
© Springer-Verlag GmbH Germany, part of Springer Nature 2023

Abstract

Landslides and ground subsidence resulting from changes in soil-water characteristics during drying and wetting cycles present a severe hazard to the environment and human life in the Loess Plateau region of China. In this study, the soil-water characteristic curve (SWCC) evolution mechanism during drying and wetting cycles was carried out on compacted loess with various dry densities. The samples were subjected to three cycles of drying-wetting, and the change of matric suction was measured using the filter paper method. Additionally, nuclear magnetic resonance (NMR) technology was used to study the change in the pore size distribution (PSD) before and after the drying-wetting cycles. The results reveal that as the dry density increased, the saturated volumetric water content decreased, the SWCC slope gradually decreased, and the air entry value increased. Furthermore, the drying-wetting cycles increased the aggregated volume and macropore diameter, and their effect on SWCC intensified with dry density. Based on experimental observation, a simple method to calculate the surface relaxivity (ρ_2) was proposed. Finally, the Weibull distribution function was innovatively applied to predict the PSD, achieving highly satisfactory accuracy. These results have practical implications for the construction and protection of loess engineering in the Loess Plateau region.

Keywords Soil-water characteristic curve (SWCC) · Nuclear magnetic resonance (NMR) · Pore size distribution (PSD) · Loess · Drying-wetting cycles

Introduction

The soil-water characteristic curve (SWCC) is a fundamental relationship between water content and matric suction that reveals the internal mechanism of unsaturated soils. The widely used “Van Genuchten model” and “Fredlund-Xing model” are commonly employed to model the SWCC (Fredlund and Xing 1994; Van Genuchten 1980).

Typically, the SWCC curve is obtained through testing a limited number of data points using methods such as the tensiometer, axial translation technique, and filter paper method. The SWCC model is then utilized to predict the entire SWCC. Matric suction plays a pivotal role in unsaturated soil mechanics, as it can predict hydraulic conductivity, soil-water storage, and shear strength of unsaturated soils (Fredlund and Rahardjo 1993; Vanapalli et al. 1999; Fredlund 2006; Lu and Likos 2006). The SWCC is influenced by various factors such as soil mineral composition, particle size gradation, density, pore structure, and organic matter (Mijares and Khire 2010; Romero et al. 2011; Jiang et al. 2017; Ma et al. 2021), all of which influence the pore structure (Beckett and Augarde 2013). As a result, the pore size distribution (PSD) of soil has a significant effect on the SWCC. Previous studies have shown that the dry density of soils significantly affects the SWCC (Eyo et al. 2022), with soils of higher dry density exhibiting greater suction for the same water content (Vanapalli et al. 1999; Birlle et al. 2008). Research results indicate that cyclic drying-wetting causes significant changes in soil cement and porosity (Aldaood et al. 2014; Goh et al. 2014; Wang et al. 2021), and pore

✉ Wankui Ni
niwankui@chd.edu.cn

Haiman Wang
2020026006@chd.edu.cn

¹ College of Geological Engineering and Geomatics, Chang'an University, Xi'an, Shaanxi 710054, People's Republic of China

² Key Lab of Western Geological Resources and Geoengineering Under Ministry of Education, Chang'an University, Xi'an, Shaanxi 710054, People's Republic of China

³ College of Architecture Engineering, HuangHuai University, Zhumadian, Henan 463000, People's Republic of China

distribution is closely related to the drying-wetting cycle (Barden et al. 1973; Bodner et al. 2013). Therefore, the effect of drying and wetting cycles on the SWCC of specimens with different dry densities is a subject of interest.

The physical properties of soil are affected by its microstructure (Liu et al. 2013), and there is a growing interest in investigating the physical properties of loess from a microstructural perspective. Differences in soil structure can cause significant variations in the soil-water characteristic curve (SWCC) of natural, remodeled, and compacted loess (Muñoz-Castelblanco et al. 2012; Ng et al. 2016; Li et al. 2018; Mu et al. 2020), with even small structural changes leading to different SWCCs in loess samples. Land transformation projects have disturbed and modified the natural loess structure of the Chinese Loess Plateau (Zhang et al. 2019a), making it imperative to develop techniques for investigating the soil pore structure and mechanical properties (Jiang et al. 2014; Li et al. 2019a). Scanning electron microscopy (SEM) and mercury intrusion porosimetry (MIP) have been used to analyze pore size distributions, particle geometric features, and morphological distribution of pores and particles in soil structure studies (Jiang et al. 2014; Li et al. 2019a). Two-dimensional (2D) images captured by scanning electron microscopy (SEM) allow a cross-sectional visual inspection of the morphological distribution of pores and particles (Li and Li 2017). MIP was used to investigate the relationship between pore size distribution and permeability of unsaturated soils (Sasanian and Newson 2013; Wang et al. 2019). However, these methods have limitations. SEM images are susceptible to human interference (Shao et al. 2018; Tang et al. 2008), while MIP has difficulty entering micropores and can damage the soil structure. Besides, the soil is more fragile than rock, and its internal structure is more complicated due to rock weathering. NMR shows promising results in testing pore size distribution, particularly for fragile and complex soil structures.

Loess, a type of soil formed under arid and semi-arid conditions, covers a large area of about 324,600 km² in north-west China (Peng et al. 2019). The implementation of the western development strategy has led to the expansion of construction activities in the loess region. For example, the Yan'an New District mega-project involved cutting mountains and filling ditches to create a flat terrain suitable for urbanization (Li et al. 2014a). As part of this project, the local government initiated a campaign in 2011 to demolish the upper part of the mountainous area and fill the river valley to create more space for subsequent urban development, resulting in the excavation and landfill of over 2273 hectares of land. The mechanical compaction of loess during this land creation process has altered its physical and mechanical properties. Although loess is relatively stable, it undergoes continuous changes between saturated and unsaturated states

due to the drying-wetting cycle of rainfall and evaporation in the region's cyclic climate system. This induces microstructural changes that affect its mechanical properties (Kong et al. 2017; Ni et al. 2020), which are crucial for predicting the stability of construction projects and slope works accurately (Kong et al. 2017; Zeng et al. 2012). Therefore, studying the microstructural changes of compacted loess under drying-wetting cycles is essential for ensuring the safety and longevity of construction projects in loess regions.

This study investigated the impact of drying-wetting cycles on the SWCC of compacted loess with different dry densities. To understand the mechanism underlying the influence of the drying-wetting cycle on SWCC at a microscopic level, the researchers used NMR to test the PSD and SEM to qualitatively analyze the microstructure of the sample before and after the drying-wetting cycle. The findings of this study led to the development of a new method for obtaining surface relaxivity (ρ_2) and a method for predicting the PSD of compacted loess with varying dry densities and drying-wetting cycles. These results and analyses provide valuable insights into the properties of unsaturated loess, which can aid in resolving geotechnical issues and mitigating geological hazards.

Materials and methods

Materials

The soil sample used in this study was collected from the Yan'an New District, located in the south-central part of the Loess Plateau in China (as shown in Fig. 1a). The sample was a Late Pleistocene (Q3) loess that had undergone mechanical compaction during the land making process in the area, leading to compacted loess with distinct properties from undisturbed loess (as shown in Fig. 1b). Soil samples were manually collected from wells buried at a depth of 2.5–3 m (as shown in Fig. 1c). To ensure the preservation of soil blocks during transportation, they were securely wrapped in black plastic bags and affixed with adhesive tape (as shown in Fig. 1d). The labeled samples were then transported to the laboratory for analysis. The key physical properties of the loess were determined using the ASTM 2013 standard test methods (Table 1).

Experimental process

The experimental process followed in this study is illustrated in Fig. 2. Initially, the samples were prepared and then subjected to SEM and matric suction tests, which required the samples to be dried and wetted until saturation, respectively.

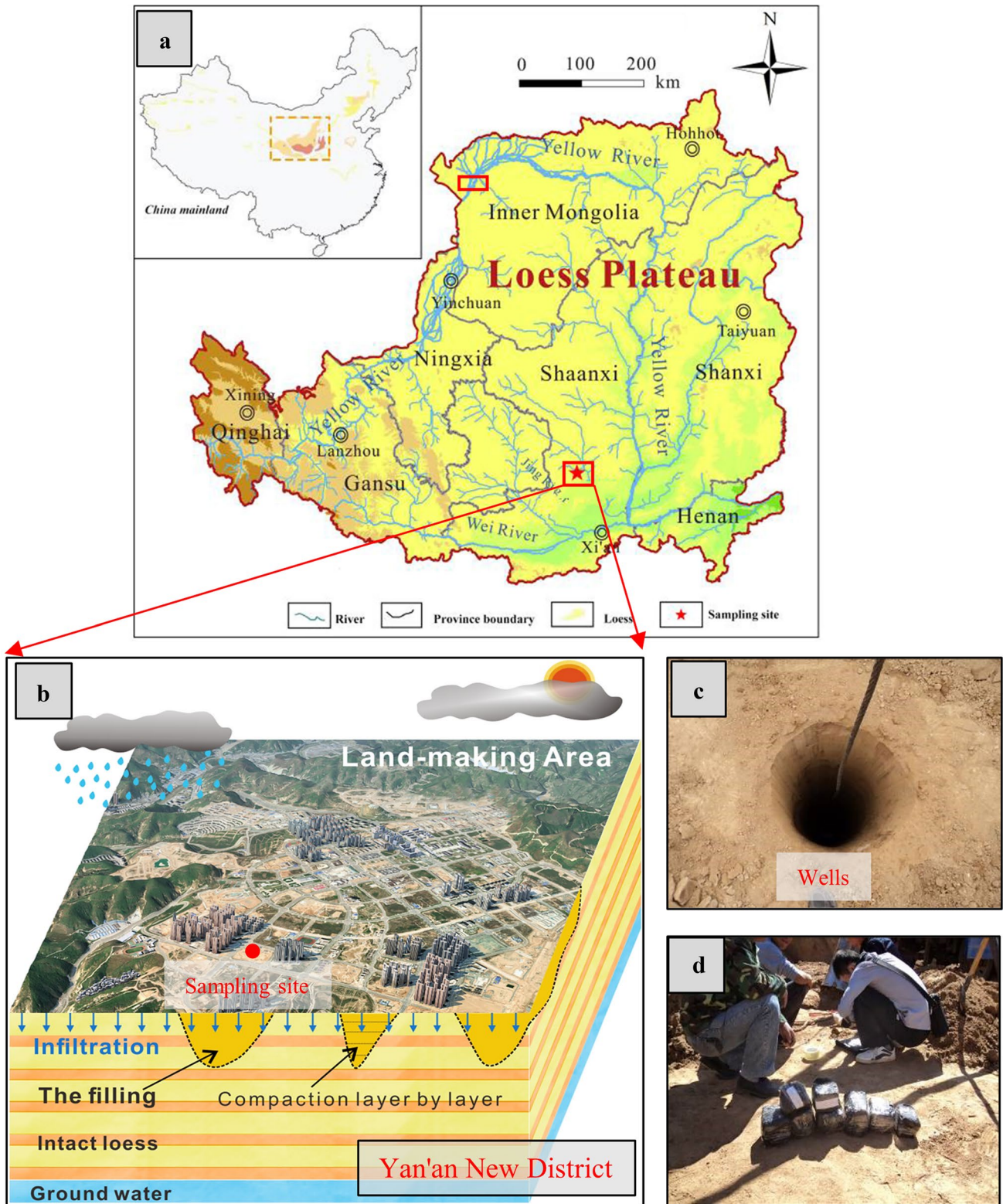


Fig. 1 a Location of the Loess Plateau (Dijkstra 2001; Hao et al. 2010), b Yan'an New District, c sampling wells, and d specimen collection

Table 1 Physical properties of the loess sample

| Property | Value |
|---------------------------------------------------|-------|
| Maximum dry density ρ_d (g/cm ³) | 1.69 |
| Natural water content w (%) | 10.12 |
| Specific gravity G_s | 2.72 |
| Liquid limit w_L (%) | 28.9 |
| Plastic limit w_p (%) | 16.1 |
| Particle size distribution | |
| Sand 0.075–2 mm (%) | 10.39 |
| Silt 0.002–0.075 mm (%) | 78.99 |
| Clay < 0.002 mm (%) | 10.62 |
| Main minerals | |
| Quartz (%) | 45.2 |
| Feldspar (%) | 21.0 |
| Calcite (%) | 15.5 |
| Dolomite (%) | 2.2 |
| Illite (%) | 4.5 |
| Chlorite (%) | 8.0 |
| Pyrite (%) | 1.9 |
| Amphibole (%) | 1.7 |

Thereafter, NMR tests were carried out on the saturated samples. Following this, the sample was subjected to three cycles of drying and wetting, as prior studies have demonstrated that the mechanical properties and microstructure of loess stabilize after the second or third cycle (Bai et al. 2021; Chen et al. 2018; Mu et al. 2018; Pan et al. 2020; Xu et al. 2020a, b; Ye et al. 2020; Zhu et al. 2022). Although the SWCC of compacted loess has not been studied directly in drying and wetting cycles, previous research has indicated that the soil microstructure controls the curve (Muñoz-Castelblanco et al. 2012; Ng et al. 2016; Li et al. 2018; Mu et al. 2020). Based on these findings, the number of cycles was set to three in this study. In addition, previous research has found that the water content of loess specimens at various depths typically reaches a minimum in the spring, but tends to remain above 10%, as reported by Xu et al. (2020a, b) and Yuan et al. (2022a, b). The drying and wetting cycles resulting from rainfall and evaporation also do not cause the water content of loess to drop below 10%, as noted by Hou et al. (2019) and Li et al. (2016). Based on these observations, it can be inferred that the specimens collected in the spring with a water content of 10.12% are likely to be close to the minimum value of water content under natural conditions. As a result, the samples were dried to a final water content of 10% at a constant temperature of 30 ± 2 °C. It is worth noting that SEM, NMR, and matric suction tests were conducted again during the third drying and wetting cycle. Further details on these tests are provided below.

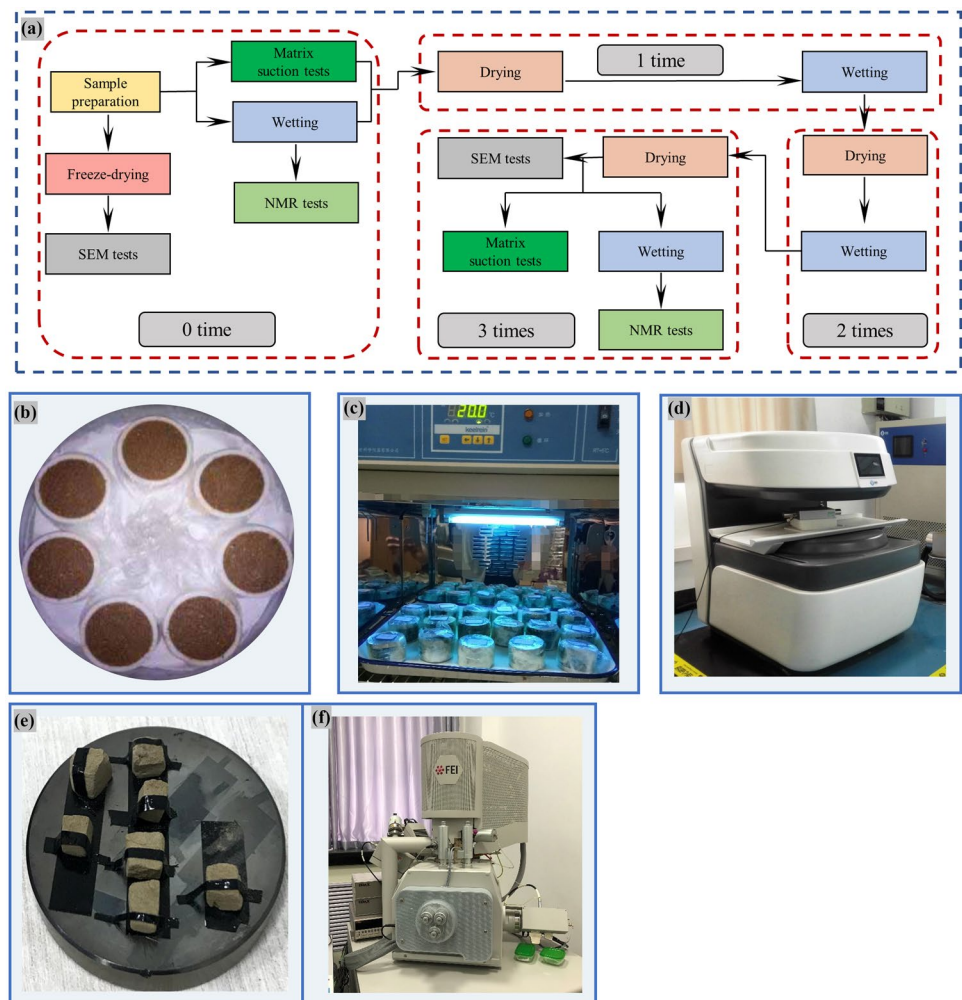
Sample preparation

Twelve loess samples for matric suction test and NMR tests were compacted to the size of 20 mm in height and 79.8 mm in diameter (Fig. 2b). Considering that the natural water content was about 10%, the maximum dry density was 1.69 g/cm³. The initial water content of the loess specimens was 10% and the dry densities were 1.45, 1.55, and 1.65 g/cm³, respectively. Four groups of samples were prepared for each dry density, and one group contains two samples. Each dry-density sample was tested in parallel to eliminate random errors.

Matric suction tests

In this study, the filter paper method was utilized to analyze the soil-water characteristic curve (SWCC). This method provides a broad testing range that can theoretically measure the entire range of matric suction while also being cost-effective, quick, and highly accurate. It also avoids damaging the soil structure, as noted by previous studies (Feuerharmel et al. 2006; Leong et al. 2002). In this experiment, Whatman No.42 slow quantitative filter papers were used. During the wetting of the specimen, distilled water was slowly and uniformly dropped onto the sample surface to ensure that the water content increases no more than 5%. To ensure the uniform distribution of water in the sample, the sample was then sealed and placed in a controlled temperature and humidity box for 3 days. Then, covered with protective filter paper, test filter paper, and another protective filter paper before being fixed together with another sample in the same group using insulating tape. Finally, samples were sealed using plastic wrap and scotch tape and placed in the box at 30 ± 2 °C for 10 days (Fig. 2c). After 10 days, equilibrium was attained, and water exchange between the soil sample and the filter paper was completed. The sealed sample was then quickly disassembled, and the filter paper was weighed. Matric suction was calculated using the mass water content of the filter paper. After the suction test was completed, these steps were repeated for the wetting and suction test. As samples were challenging to be saturated under atmospheric conditions, vacuum saturation was undertaken when the water content was close to saturation. During this experiment, permeable stones and filter paper were placed on the top and bottom of the samples to prevent sample damage during the saturating process. After the saturated samples were weighed, a Mini NMR nuclear magnetic resonance analyzer (Model PQ-001; Suzhou Newmai Company) was used to conduct NMR analysis (Fig. 2d).

Fig. 2 **a** Experimental flow chart, **b** prepared specimen, **c** matrix suction test, **d** NMR analyzer, **e** SEM specimen, and **f** SEM equipment



NMR tests

NMR technology is a non-destructive and rapid method for measuring the distribution of hydrogen protons per unit volume (Callaghan et al. 1991). The hydrogen proton distribution can be indirectly used to determine the pore distribution in loess samples as the pores in saturated samples are filled with water. It is worth noting that the presence of ferromagnetic materials, such as traditional stainless steel ring knives, can adversely affect the uniformity of the main magnetic field in the NMR analyzer. Therefore, in this study, a PTFE ring knife was used instead of a traditional stainless steel one (Fig. 2b). Furthermore, to facilitate the investigation of the particle size distribution (PSD) in the soil, the pores were assumed to be cylindrical in shape (Tian et al. 2014). The relationship between the pore diameter (d) and the proton spin–spin relaxation time (T_2) can be expressed as shown by Coates et al. (1999):

$$d = 4 \cdot T_2 \cdot \rho_2 \tag{1}$$

where ρ_2 is the T_2 surface relaxivity (um/ms). ρ_2 is a constant for specific soil composition and is independent of temperature and pressure (Tian and Wei 2014), but it varies with soil mineral composition. T_2 is directly proportional to pore diameter; therefore, it can be used to represent pore diameter (Eq. (1)). Additionally, Ishizaki et al. (1996) noted that the nuclear magnetic signal curve was directly proportional to sample water content, which allows the characterization of the pore volume in the sample. In summary, the NMR technology offers an effective means to measure the content of various pores in loess samples.

Methods such as MIP and nitrogen adsorption were previously used to solve the ρ_2 (Srland et al. 2007; Yao and Liu 2012); the Schlumberger-Doll Research (SDR) equation developed by Kenyon et al. (1988) and used in this study to solve the surface relaxation strength ρ_2 is a simple and widely accepted method.

$$k_s = C\phi^4 T_{2LM}^2 \tag{2}$$

where k_s is the saturated permeability of the soil; \emptyset is porosity; T_{2LM} is the geometric mean of the T_2 distribution. As the constant C in the SDR equation is proportional to the square of the surface relaxation intensity (Kleinberg et al. 2003) ($C = \rho_2^2$), Eq. (2) can be expressed as:

$$k_s = \rho_2^2 \emptyset^4 T_{2LM}^2 \tag{3}$$

ρ_2 can be expressed as:

$$\rho_2 = \sqrt{\frac{k_s}{\emptyset^4 T_{2LM}^2}} \tag{4}$$

where k_s is $1.18 \times 10^{-13} \text{m}^2$; \emptyset is 0.49; T_{2LM} is 0.52989 ms, ρ_2 is 2.69 $\mu\text{m}/\text{ms}$ for samples with a dry density of $1.45 \text{g}/\text{cm}^3$. By substituting the value of ρ_2 into Eq. (1), the T_2 curve can be converted into a pore distribution curve. Pore distribution curves in this study were all converted from the T_2 curve using this method.

SEM tests

To ensure that the soil sample structure was not disturbed during NMR testing, the surface soil of the intact block sample was uniformly and carefully trimmed off. A cubic stick measuring $10 \text{mm} \times 10 \text{mm} \times 20 \text{mm}$ (L \times W \times H) was then cut from the core of the intact block sample (Fig. 2e). The conventional air-drying method can cause soil samples

to shrink and deform. Therefore, in this study, sticks were dehydrated using a freeze dryer with liquid nitrogen at a temperature below $-70 \text{ }^\circ\text{C}$ to minimize the possible influence of water on subsequent microstructure observations (Wei et al. 2020). Before microstructural observation, each soil stick was fractured carefully to be approximately 10 mm in height. One-half stick was stuck to the shooting pad using electron-conductive tape without disturbing the fractured plane. The selected fractured plane was sputter-coated with platinum (i.e., Pt) in a piece of sputtering ion equipment and used for microstructural observation through an FEI MLA650F scanning electron microscope (Fig. 2f).

Results and discussion

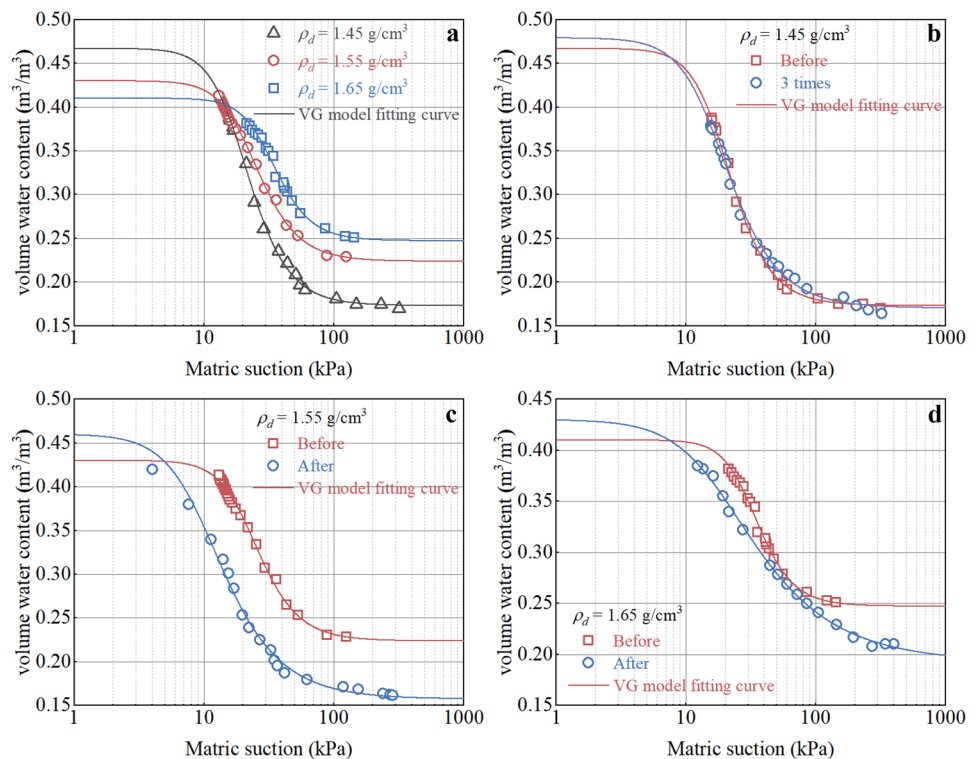
SWCC of samples before and after the drying-wetting cycle

Among numerous fitted SWCC models, the VG model is the most widely used for unsaturated loess. In this study, experimental data were fitted using the VG model as follows:

$$S_e = \frac{\theta - \theta_r}{\theta_s - \theta_r} = \left[\frac{1}{1 + (a\psi)^n} \right]^m \tag{5}$$

where S_e represents effective saturation; θ is the current water content; θ_r is the residual water content; θ_s is the saturated

Fig. 3 SWCCs before and after drying-wetting cycles fitted by VG model. **a** Before drying-wetting cycles. **b** $\rho_d = 1.45 \text{g}/\text{cm}^3$. **c** $\rho_d = 1.55 \text{g}/\text{cm}^3$. **d** $\rho_d = 1.65 \text{g}/\text{cm}^3$



volume water content; ψ is the matric suction (kPa); a , m , and n are fitting parameters, in which a is the function of the air entry value, generally considered $m = 1 - 1/n$.

The determination of θ_s was carried out through vacuum saturation, while θ_r was obtained through fitting as experimental results from different methods yielded inconsistent values due to nonuniform standards. By sorting and fitting the data obtained from the tests in Fig. 3, SWCCs of compacted loess with varying dry densities were obtained.

The VG model was employed to fit the SWCCs of compacted loess samples with different dry densities, and the fitting correlation coefficients (R^2) were all above 0.98, indicating that the model is effective in fitting the SWCC of loess. With an increase in dry density, the saturated water content decreased, and the SWCC slope gradually decreased (Gallage and Uchimura 2010). Additionally, the air entry value of the SWCC also increased (Fig. 3a) (Kawai et al. 2020).

After the drying-wetting cycle, the samples exhibited varying degrees of increase in saturated water content, while the air entry value decreased (Fig. 3), suggesting an increase in porosity ratio and maximum pore diameter. The overlapping SWCCs of the sample with a dry density of 1.45 g/cm³ before and after the drying-wetting cycle suggest minimal impact on the pores. The parallel transition section of the SWCC of the sample with a dry density of 1.55 g/cm³ before and after the drying-wetting cycle indicates a significant impact. The significant change in the shape of the SWCC of the sample with a dry density of 1.65 g/cm³ suggests that the

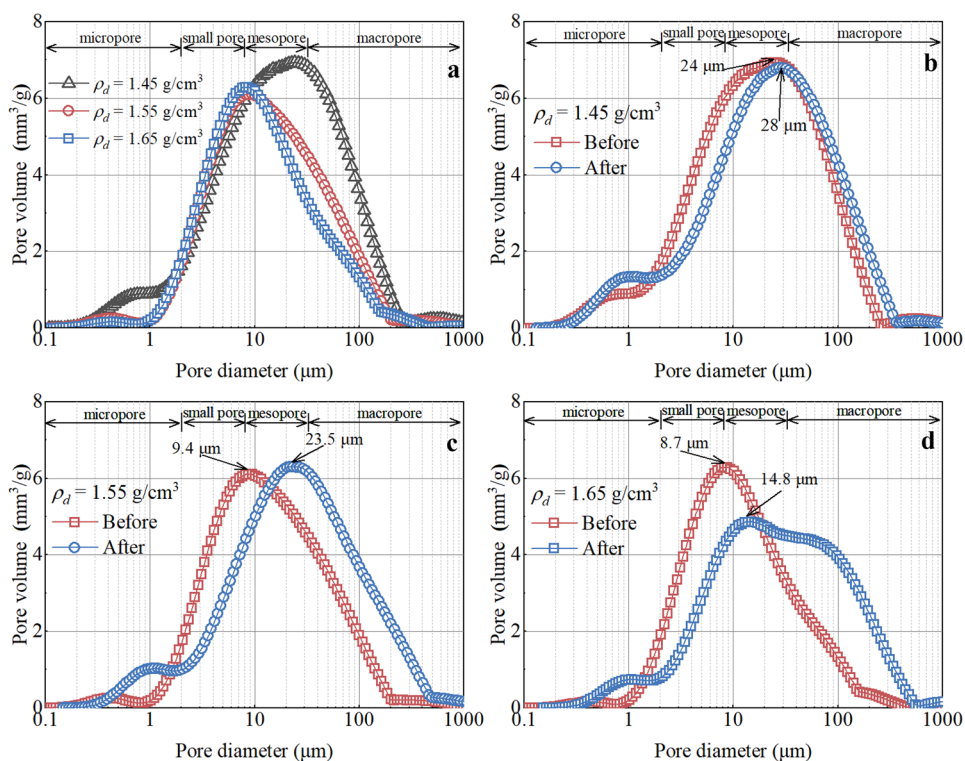
effect of the drying-wetting cycle on SWCC increases with an increase in dry density.

Pore distribution characteristics of the samples

The pore size distribution frequency (PSDF) has a decisive influence on the SWCC. In order to study the influence of the drying-wetting cycle on the pore structure of loess, the distribution curve T_2 of the sample was transformed into a pore size density function curve in Fig. 4.

Figure 4 illustrates the pore size distribution frequency (PSDF) for different dry-density specimens before and after undergoing drying-wetting cycles. The PSDF of specimens that has not undergone drying-wetting cycles is significantly affected by the dry density, as indicated in Fig. 4a. For the specimen with a dry density of 1.45 g/cm³, the PSDF showed a bimodal characteristic with two peaks at diameters of 0.6 μ m and 24 μ m, respectively. The pore diameter corresponding to the larger peak is defined here as the dominant pore diameter (d_a). When the dry density increased to 1.55 g/cm³, the peak at 0.6 μ m decreased almost entirely, and d_a reduced dramatically from 24 to 9.4 μ m (Wang et al. 2019). The shape of the curve remained the same as the dry density increased from 1.55 to 1.65 g/cm³, but there was a significant reduction in the volume of pores with diameters larger than 10 μ m. In general, the effect of dry density on the PSDF of specimens decreased as the dry density increased. It is important to note that the PSDF curves for pore sizes less

Fig. 4 Pore size distribution frequency curve. **a** Before drying-wetting cycles. **b** $\rho_d = 1.45$ g/cm³. **c** $\rho_d = 1.55$ g/cm³. **d** $\rho_d = 1.65$ g/cm³



than 0.2 μm overlapped, indicating that compaction did not have a substantial effect on this pore range, which is consistent with the findings of Ng et al. (2016).

The PSDF of specimens is also influenced by drying-wetting cycles, as noted by Yuan et al. (2022a, b). Figure 4b indicates that drying-wetting cycles did not alter the bimodal properties for a dry density of 1.45 g/cm³, but the smaller peak increased, and d_a slightly increased from 24 to 28 μm. Overall, drying-wetting cycles had a minimal impact on the PSDF of specimens with a dry density of 1.45 g/cm³. As demonstrated in Fig. 4c, the effect of drying-wetting cycles on the specimen with a dry density of 1.55 g/cm³ was more pronounced than on the specimen with a dry density of 1.45 g/cm³. After the drying-wetting cycles, the PSDF curve produced a new peak at a pore size of 1 μm. Additionally, d_a significantly increased from 9.4 to 23.5 μm. For the specimen with a dry density of 1.65 g/cm³, the drying-wetting cycles produced a new peak at a pore size of 1 μm and altered the shape of the PSDF curve (Fig. 4d). Overall, the effect of drying-wetting cycles on the PSDF curves of specimens increased with increasing dry density, which corresponds to the impact of drying-wetting cycles on SWCC demonstrated in Fig. 3.

In order to explore the correlation between d_a and e (dry density), Fig. 5 illustrates the d_a and e values of the specimens before and after drying-wetting cycles. It can be observed that, in logarithmic coordinates, there is a linear relationship between e and d_a , as previously reported by Phadnis and Santamarina (2011), which is also compared with the research by Wang et al. (2019). Notably, the slope of the linear relationship between e and d_a appears to be consistent across various soils, with differences only observed in the intercepts.

The void ratio (e) was calculated, and the NMR test was performed. According to Eq. (1), there is a unique correspondence between d and T_2 , and d_a can be expressed as:

$$d_a = 4T_{2p} \rho_2 \tag{6}$$

where T_{2p} is the T_2 corresponding to the peak point of the T_2 curve; by substituting the relational expression of d_a and e of Yan'an compacted loess in Fig. 5, ρ_2 can be calculated by measuring samples e and T_{2p} . The specific formula is as follows:

$$\rho_2 = \frac{10^{\frac{\text{Log}e+0.3579}{0.216}}}{4 T_{2p}} \tag{7}$$

The ρ_2 can be obtained by measuring the void ratio of the sample after the NMR test. Because the intercepts of the curves in Fig. 5 are different for various loess, Eq. (7) is only applicable to Yan'an compacted loess.

Li et al. (2020) posited that the inter-aggregate pores in loess follow a normal distribution, which implies that pores smaller than the dominant pore diameter are roughly equivalent to half of the total inter-aggregate pore volume. This study also confirms that the PSD curve for the entire sample is symmetric around the dominant pore diameter, but the micropores exhibit discernible dissimilarities. The volume of micropores only occupies a small part of the total pore volume, so the asymmetry of the micropores can be ignored. The pore volume whose pore size is smaller than the dominant pore diameter (V_L) is equal to half of the total pore volume ($V_S/2$) (Fig. 6).

Pores were divided into four categories to analyze pore volume and pore size quantitatively: micropores ($d < 2 \mu\text{m}$), small pores ($2 < d < 8 \mu\text{m}$), mesopores ($8 < d < 32 \mu\text{m}$), and macropores ($d > 32 \mu\text{m}$) (Lei 1988). Various pore volume statistics were obtained by calculating various pore volumes in Fig. 7.

The results presented in Fig. 7 demonstrate that the increase in dry density leads to a reduction in the volume

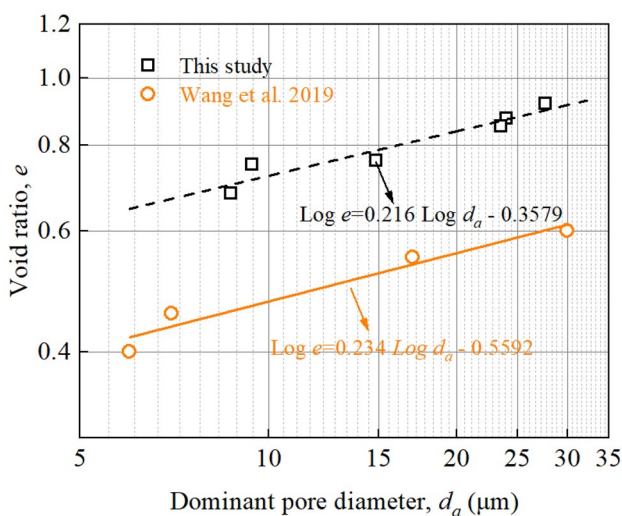


Fig. 5 Relationship between void ratio and dominant pore diameter

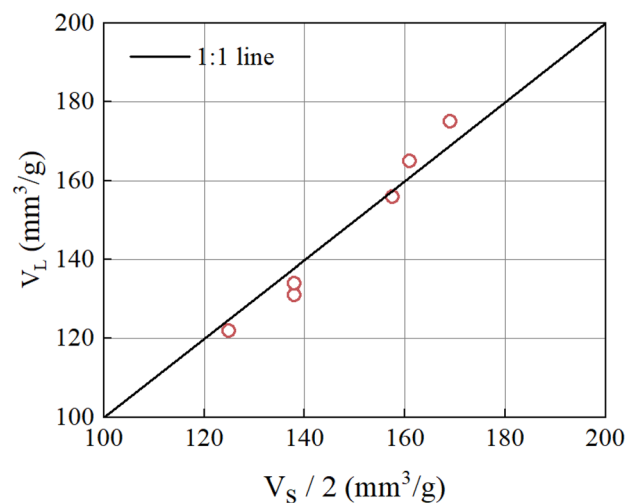


Fig. 6 Comparison between V_L and $V_S/2$ determined by NMR

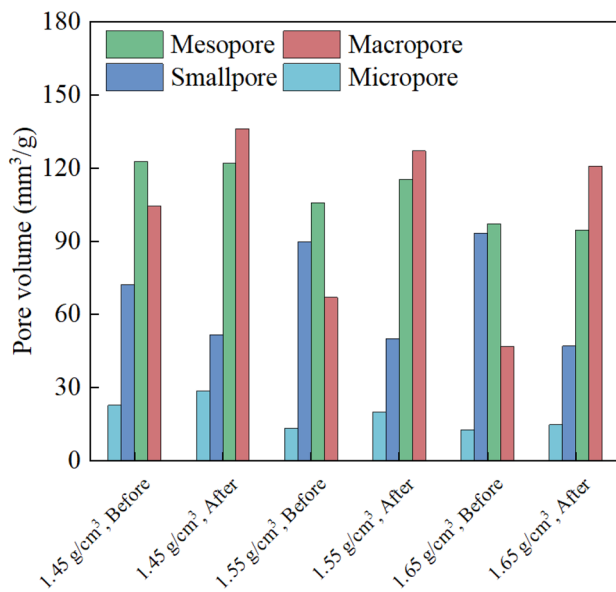


Fig. 7 Pore composition of different types

of macropores and mesopores (dominant pores), while the volume of small pores increases gradually. The increase in dry density of the specimen can be regarded as a process of compression, indicating that the macropore and mesopore damage will be partially transformed into small pores during the compression of the loess specimen. Additionally, the volume of micropores decreases significantly when the dry density increases from 1.45 to 1.55 g/cm³. However, no further changes in micropore volume were observed for the sample with a dry density of 1.65 g/cm³, suggesting that compression does not produce micropores beyond a certain threshold. This finding contradicts previous studies that reported constant micropore volumes during compression (Li et al. 2020; Wang et al. 2019; Zhang et al. 2019b). The observed phenomenon can be attributed to several factors, including (I) the compacted loess is dried and crushed during the preparation process so that the cemented material in the aggregates is destroyed; (II) on the dry side in the best state, there was not enough water to absorb the double electron layer on the clay surface; (III) a sample with a lower dry density has a larger micropores volume, which can lead aggregates to be destroyed during compression (Azizi et al. 2019; Li et al. 2019b); (IV) there is currently no unified standard for pore classification.

Following the drying-wetting cycle, the dominant pore in all samples shifted from mesopores to macropores, while the number of small pores decreased, suggesting that small pores underwent growth to become larger pores (Fig. 7). In addition, micropore volume increased across all samples. Notably, the sample with a dry density of 1.45 g/cm³ exhibited the least significant change in pore volume compared to the samples with dry densities of 1.55 and 1.65 g/cm³.

The SWCC is influenced by various factors, including mineral composition, pore structure, shrinkage, and stress history. In the case of a specific type of soil, the water loss state and the associated matric suction are solely determined by the number and size of its pores. Hence, the SWCC can serve as an indirect indicator of the PSD of the soil. To elucidate the influence of macropores on the air entry value, the Young–Laplace equation was introduced:

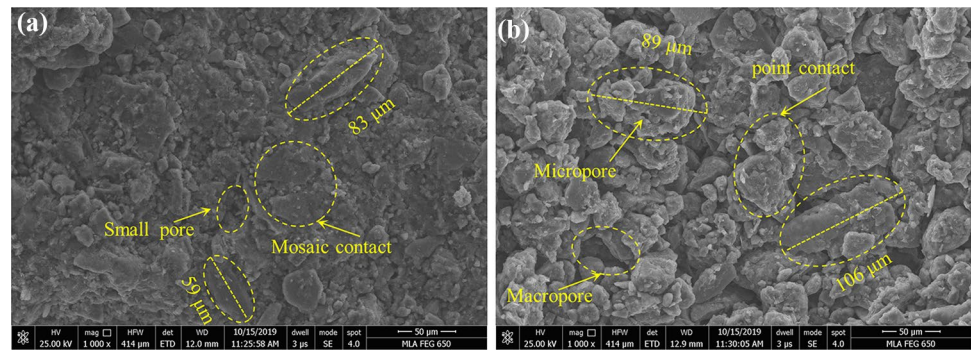
$$\psi = \frac{4T_s \cos \alpha}{d} \quad (8)$$

where T_s is the surface tension on the water–gas interface, and α is the contact angle between soil particles and pore water, generally being 0°. Specimens with low dry density exhibit a higher proportion of macropores, which, according to Fig. 7, allows the soil to start losing water rapidly at a smaller suction condition (Eq. (8)). Consequently, the air entry value of such specimens is lower, and the saturated water content is higher, as shown in Fig. 3. The slope of the SWCC is an indicator of the rate of change of water content with matric suction, with steeper slopes indicating a more rapid loss of soil water. Lower dry-density specimens have larger dominant pore volumes, which result in a gradual decrease in the slope of the SWCC with increasing dry density, as observed in Fig. 3 (Li and Li 2017; Zhao and Wang 2012). Figure 7 illustrates that not only did the volume of macropores increase following the drying and wetting cycles, but the dominant pore size also changed from mesopores to macropores. Additionally, the impact of drying and wetting cycles on the specimens was more pronounced with increasing dry density. Therefore, the saturated volumetric water content of the specimens and the slope of the SWCC increased after the drying and wetting cycles, while the air entry value decreased, and this trend intensified with higher dry densities, as evidenced in Fig. 3.

Microstructure characteristics of drying-wetting cycle specimens

After drying-wetting cycles, the specimens with void ratios of 1.45, 1.55, and 1.65 g/cm³ increased by 5.7%, 8.6%, and 13.3%. The sample with a dry density of 1.65 g/cm³ was taken as an example because its porosity changed the most before and after the drying-wetting cycle. Figure 8 shows the SEM images before and after the dry–wet cycle with a dry density of 1.65 g/cm³. The drying-wetting cycle will cause a change in the accumulation arrangement of clay particles, and thus the change of microstructure (Allam and Sridharan 1981). Figure 8a shows that before the drying-wetting cycle, the primary contact between aggregates in the compacted loess is the mosaic structure. The

Fig. 8 SEM images before and after the dry-wet cycle with a dry density of 1.65 g/cm³. **a** Before. **b** After



aggregates are bonded together, and the pore connectivity is poor. After the drying-wetting cycle, the samples have a higher void ratio, the contact form between the aggregates becomes the brack contact, and the contour of the aggregates is more apparent, as shown in Fig. 8b. The contact form of aggregates suggests that the water dissolves the cementitious material in the drying-wetting cycle, resulting in the macropores after some small pores and mesopores being connected, which makes the soil have a high void ratio. At the same time, it is found that the aggregate size of the soil increased after the drying-wetting cycle due to the irreversible van der Waals force, which makes the clay close to the aggregate and agglomerates into larger aggregates (Day 1994). During the accumulation of clay particles, the drying-wetting cycle will increase the micropores because the clay particles cannot be densely contacted. The increase of aggregates means that the specific surface area decreases, the pores between aggregates, and the volume of macropores becomes larger.

The aforementioned analysis reveals that the SWCC of specimens is affected by drying and wetting cycles via two mechanisms: (I) during the cycle water enters the cement, and the corrosive effect increases the pore size of both small and mesopores and increases their connectivity (Zhao and Wang 2012); (II) under the influence of van der Waals forces, clay particles approach agglomerates to form larger intergranular pores. Thus, the diameter and number of macropores and the connectivity between pores of the specimens increased significantly after the drying and wetting cycles, resulting in an increase in saturated water content, a decrease in air entry value, and an increase in SWCC slope, which is consistent with Fig. 3. Furthermore, for specimens with higher dry density, the corrosive effect and the agglomeration of clay particles are more pronounced due to the greater number of small pores in the interior, resulting in a more significant effect of drying and wetting cycles on SWCC as dry density increases, as shown in Fig. 3.

PSD evolution model of compacted loess

It has been widely believed that overall shape of PSDF curves remains unchanged during deformation and is identical to the initial state (Cheng et al. 2019; Hu et al. 2013; Li et al. 2014b). However, this study has discovered that the PSDF shape changes during compression and the drying-wetting cycle (Fig. 4). Therefore, a versatile model is needed to simulate the evolution of PSD. The Weibull distribution function is a suitable model as it is controlled by scale and shape parameters, making it adaptable to various shapes, and it is widely used in production activities (Gallage and Uchimura 2010). The cumulative distribution function can be expressed as:

$$F(x) = 1 - e^{-(x/a)^n} \quad (9)$$

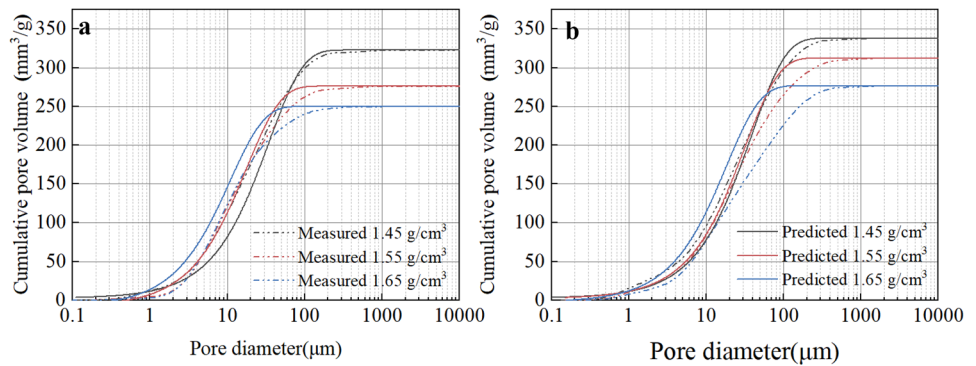
where a and n are the scale and shape parameters of Weibull distribution, respectively. At a pore diameter of zero, the cumulative pore volume is also zero, and at a large enough diameter, the cumulative pore volume is equal to the total volume. Therefore, the Weibull cumulative distribution function can be modified to the PSD model (hereinafter referred to as the Weibull model):

$$V(d) = V_s [1 - 0.5 \times e^{-((d-a)/(a+d_a/2-1))^n}] \quad (10)$$

where d is the pore diameter (μm); $V(d)$ is the pore volume with a pore diameter less than d (mm^3/g); V_s represents the total pore volume (mm^3/g). The modified Weibull model is still controlled by two parameters a and n , so it can be used to simulate various PSD curves. Since the dominant diameter (d_a) corresponds to the extreme point of the PSDF curve, the second derivative of the Weibull model at d_a is zero, that is, $V''(d)|_{d=d_a} = 0$. After simplification, we can get:

$$\frac{n-1}{n} = \left(\frac{d_a - a}{a + d_a/2 - 1} \right)^n \quad (11)$$

Fig. 9 Comparison between measured and predicted PSDs. **a** Before drying-wetting cycles. **b** After drying-wetting cycles



After substituting $V(d_a) = V_S/2$ (Fig. 6) into Eq. (10):

$$\ln\left(\frac{0.5V_S}{V_S - V(d_a)}\right) = \left(\frac{d_a - a}{a + d_a/2 - 1}\right)^n = 0 \tag{12}$$

Based on Eqs. (11) and (12), the solutions of parameters a and n can be obtained:

$$n = 1; a = d_a \tag{13}$$

Based on the empirical formula shown in Fig. 5, d_a can be easily obtained when the void ratio of compacted loess is known. Then according to Eq. (13), the scale parameter (a) and shape parameter (n) can be solved, then the PSD curve can be drawn.

The comparison between the measured and predicted PSDs of samples with varying dry densities depicted in Fig. 9 demonstrates a good agreement. The proposed model can effectively predict the PSD of samples subjected to cycle of drying and wetting. Notably, the accuracy of prediction for samples before the drying-wetting cycle is significantly higher than that of samples after the cycle. The discrepancies between the predicted and measured curves can arise from two aspects: firstly, d_a is determined through the empirical equation shown in Fig. 5, thus introducing error into a ; secondly, the assumption that the pore volume whose size is smaller than the dominant pore size is equal to half of the total pore volume may introduce error into the shape parameter, n . Furthermore, the model may not be able to provide different PSDs for two compacted loess samples with the same e , as d_a is determined by the relationship between e and d_a , and the parameter a is also related to d_a . This issue is common to other models as well (Cheng et al. 2019; Hu et al. 2013). However, the major strength of this model is that the shape of the PSD curve is not pre-determined, but rather solved based on the mathematical model, which is consistent with the experimental outcomes.

Conclusions

In this study, the evolution of SWCC and PSD of compacted loess subjected to drying-wetting cycles was investigated using NMR and SEM techniques. This comprehensive study can draw some important conclusions.

The air entry value of SWCC is mainly controlled by the macropores diameter, while the slope is mainly determined by the dominant pore volume. As the dry density increases, the air entry value increases, and the SWCC curve gradually flattens. During compression, the macropores and mesopores are compressed to produce small pores, while the micropores of the lower dry-density sample gradually close during compression and remain constant after reaching a certain value.

After the drying-wetting cycle, the dominant pores shift from mesopores to macropores, leading to a decrease in the SWCC air entry value. However, small pores are significantly reduced, indicating that some small pores grow into macropores during the drying-wetting cycle due to the dissolution of colloidal material caused by water and the action of van der Waals force. Additionally, the void ratios of specimens with dry densities of 1.45, 1.55, and 1.65 g/cm³ increased by 5.7%, 8.6%, and 13.3%, respectively, after drying-wetting cycles. The effect of drying-wetting cycles on SWCC increases with an increase in dry density.

The linear relationship between the void ratio and the dominant pore size was observed in logarithmic coordinates, and the slope was found to be 0.216 for different soils but with different intercepts. Based on this relationship, the Weibull distribution function was introduced to predict PSD, and the proposed model could predict the PSD of compacted loess at any density by obtaining e through simple experiments.

Funding The authors gratefully acknowledge the Key Program of the National Natural Science Foundation of China (Grant no. 41931285), and the key research and development program of Shaanxi Province (Grant no. 2020SF-436).

Data availability The data that support the findings of this study are available from the corresponding author upon reasonable request.

References

- Aldaood A, Bouasker M, Al-Mukhtar M (2014) Impact of wetting–drying cycles on the microstructure and mechanical properties of lime-stabilized gypseous soils. *Eng Geol* 174:11–21. <https://doi.org/10.1016/j.enggeo.2014.03.002>
- Allam MM, Sridharan A (1981) Effect of wetting and drying on shear strength. *J Geotech Eng Div* 107:421–438. [https://doi.org/10.1016/0148-9062\(81\)90058-9](https://doi.org/10.1016/0148-9062(81)90058-9)
- Azizi A, Musso G, Jommi C (2019) Effects of repeated hydraulic loads on microstructure and hydraulic behaviour of a compacted clayey silt. *Can Geotech J* 57:100–114. <https://doi.org/10.1139/cgj-2018-0505>
- Bai Y, Ye W, Wu Y, Chen Y (2021) Multiscale analysis of the strength deterioration of loess under the action of drying and wetting cycles. *Adv Mater Sci Eng* 2021:6654815. <https://doi.org/10.1155/2021/6654815>
- Barden L, McGown A, Collins K (1973) The collapse mechanism in partly saturated soil. *Eng Geol* 7:49–60. [https://doi.org/10.1016/0013-7952\(73\)90006-9](https://doi.org/10.1016/0013-7952(73)90006-9)
- Beckett CTS, Augarde CE (2013) Prediction of soil water retention properties using pore-size distribution and porosity. *Can Geotech J* 50:435–450. <https://doi.org/10.1139/cgj-2012-0320>
- Birle E, Heyer D, Vogt N (2008) Influence of the initial water content and dry density on the soil-water retention curve and the shrinkage behavior of a compacted clay. *Acta Geotech* 3:191. <https://doi.org/10.1007/s11440-008-0059-y>
- Bodner G, Scholl P, Kaul HP (2013) Field quantification of wetting–drying cycles to predict temporal changes of soil pore size distribution. *Soil Tillage Res* 133:1–9. <https://doi.org/10.1016/j.still.2013.05.006>
- Callaghan PT, Coy A, MacGowan D, Packer KJ, Zelaya FO (1991) Diffraction-like effects in NMR diffusion studies of fluids in porous solids. *Nature* 351:467–469. <https://doi.org/10.1038/351467a0>
- Chen R, Xu T, Lei W, Zhao Y, Qiao J (2018) Impact of multiple drying–wetting cycles on shear behaviour of an unsaturated compacted clay. *Environ Earth Sci* 77:683. <https://doi.org/10.1007/s12665-018-7868-6>
- Cheng Q, Ng CWW, Zhou C, Tang CS (2019) A new water retention model that considers pore non-uniformity and evolution of pore size distribution. *B Eng Geol Environ* 78:5055–5065. <https://doi.org/10.1007/s10064-019-01476-4>
- Coates GR, Xiao L, Prammer MG (1999) NMR logging principles and interpretation. Halliburton Energy Service, Houston, Texas
- Day RW (1994) Swell-shrink behavior of compacted clay. *J Geotech Eng* 120:618–623. [https://doi.org/10.1061/\(ASCE\)0733-9410\(1994\)120:3\(618\)](https://doi.org/10.1061/(ASCE)0733-9410(1994)120:3(618))
- Dijkstra TA (2001) Geotechnical thresholds in the Lanzhou loess of China. *Quatern Int* 76–77:21–28. [https://doi.org/10.1016/S1040-6182\(00\)00086-0](https://doi.org/10.1016/S1040-6182(00)00086-0)
- Eyo EU, Ng’Ambi S, Abbey SJ (2022) An overview of soil-water characteristic curves of stabilised soils and their influential factors. *J King Saud Univ Eng Sci* 34:31–45. <https://doi.org/10.1016/j.jksues.2020.07.013>
- Feuerharmel C, Gehling WYY, Bica AVD (2006) The use of filter-paper and suction-plate methods for determining the soil-water characteristic curve of undisturbed colluvium soils. *Geotech Test J* 29:419–425. <https://doi.org/10.1520/GTJ14004>
- Fredlund DG (2006) Unsaturated soil mechanics in engineering practice. *J Geotech Geoenviron* 132:286–321. [https://doi.org/10.1061/\(ASCE\)1090-0241\(2006\)132:3\(286\)](https://doi.org/10.1061/(ASCE)1090-0241(2006)132:3(286))
- Fredlund DG, Rahardjo H (1993) Soil mechanics for unsaturated soils. John Wiley & Sons
- Fredlund DG, Xing A (1994) Equations for the soil-water characteristic curve. *Can Geotech J* 31:521–532. <https://doi.org/10.1139/94-061>
- Gallage CPK, Uchimura T (2010) Effects of dry density and grain size distribution on soil-water characteristic curves of sandy soils. *Soils Found* 50:161–172. <https://doi.org/10.3208/sandf.50.161>
- Goh SG, Rahardjo H, Leong EC (2014) Shear strength of unsaturated soils under multiple drying–wetting cycles. *J Geotech Geoenviron* 140:6013001. [https://doi.org/10.1061/\(ASCE\)GT.1943-5606.0001032](https://doi.org/10.1061/(ASCE)GT.1943-5606.0001032)
- Hao Q, Guo Z, Qiao Y, Xu B, Oldfield F (2010) Geochemical evidence for the provenance of middle Pleistocene loess deposits in southern China. *Quaternary Sci Rev* 29:3317–3326. <https://doi.org/10.1016/j.quascirev.2010.08.004>
- Hou X, Li T, Vanapalli SK et al (2019) Water percolation in a thick unsaturated loess layer considering the ground-atmosphere interaction. *Hydrol Process* 33:794–802. <https://doi.org/10.1002/hyp.13364>
- Hu R, Chen YF, Liu HH, Zhou CB (2013) A water retention curve and unsaturated hydraulic conductivity model for deformable soils: consideration of the change in pore-size distribution. *Géotechnique* 63:1389–1405. <https://doi.org/10.1680/geot.12.P.182>
- Ishizaki T, Maruyama M, Furukawa Y, Dash JG (1996) Premelting of ice in porous silica glass. *J Cryst Growth* 163:455–460. [https://doi.org/10.1016/0022-0248\(95\)00990-6](https://doi.org/10.1016/0022-0248(95)00990-6)
- Jiang MJ, Li T, Hu HJ, Thornton C (2014) DEM analyses of one-dimensional compression and collapse behaviour of unsaturated structural loess. *Comput Geotech* 60:47–60. <https://doi.org/10.1016/j.compgeo.2014.04.002>
- Jiang Y, Chen W, Wang G, Sun G, Zhang F (2017) Influence of initial dry density and water content on the soil-water characteristic curve and suction stress of a reconstituted loess soil. *B Eng Geol Environ* 76:1085–1095. <https://doi.org/10.1007/s10064-016-0899-x>
- Kawai K, Kato S, Karube D (2020) The model of water retention curve considering effects of void ratio. *Unsaturated soils for Asia*. CRC Press, pp 329–334
- Kenyon WE, Day PI, Straley C, Willemsen JF (1988) A three-part study of NMR longitudinal relaxation properties of water-saturated sandstones. *SPE Form Eval* 3:622–636. <https://doi.org/10.1021/18/15643-pa>
- Kleinberg RL, Flaum C, Griffin DD, Brewer PG, Malby GE, Peltzer ET, Yesinowski JP (2003) Deep sea NMR: methane hydrate growth habit in porous media and its relationship to hydraulic permeability, deposit accumulation, and submarine slope stability. *J Geophys Res Solid Earth* 108:2508. <https://doi.org/10.1029/2003JB002389>
- Kong L, Sayem HM, Tian H (2017) Influence of drying–wetting cycles on soil-water characteristic curve of undisturbed granitic residual soils and microstructure mechanism by nuclear magnetic resonance (NMR) spin-spin relaxation time (T₂) relaxometry. *Can Geotech J* 55:208–216. <https://doi.org/10.1139/cgj-2016-0614>
- Lei XY (1988) The types of loess pores in china and their relationship with collapsibility. *Sci China Chem* 31(11):1398–1411
- Leong EC, He L, Rahardjo H (2002) Factors affecting the filter paper method for total and matric suction measurements. *Geotech Test J* 25(3):322–333. <https://doi.org/10.1520/GTJ11094J>
- Li XA, Li L (2017) Quantification of the pore structures of Malan loess and the effects on loess permeability and environmental significance, Shaanxi Province, China: an experimental study. *Environ Earth Sci* 76:523. <https://doi.org/10.1007/s12665-017-6855-7>
- Li P, Qian H, Wu J (2014a) Environment: accelerate research on land creation. *Nature* 510(7503):29–31. <https://doi.org/10.1038/510029a>
- Li X, Zhang L, Wu L (2014b) A framework for unifying soil fabric, suction, void ratio, and water content during the dehydration process. *Soil Sci Soc Am J* 78:387–399. <https://doi.org/10.2136/sssaj2013.08.0362>
- Li P, Li T, Vanapalli SK (2016) Influence of environmental factors on the wetting front depth: a case study in the Loess Plateau. *Eng Geol* 214:1–10. <https://doi.org/10.1016/j.enggeo.2016.09.008>

- Li P, Li T, Vanapalli SK (2018) Prediction of soil-water characteristic curve for Malan loess in Loess Plateau of China. *J Cent South Univ* 25:432–447. <https://doi.org/10.1007/s11771-018-3748-1>
- Li P, Xie W, Pak RYS, Vanapalli SK (2019a) Microstructural evolution of loess soils from the Loess Plateau of China. *CATENA* 173:276–288. <https://doi.org/10.1016/j.catena.2018.10.006>
- Li X, Li L, Song Y, Hong B, Wang L, Sun J (2019b) Characterization of the mechanisms underlying loess collapsibility for land-creation project in Shaanxi Province, China—a study from a micro perspective. *Eng Geol* 249:77–88. <https://doi.org/10.1016/j.enggeo.2018.12.024>
- Li P, Shao S, Vanapalli SK (2020) Characterizing and modeling the pore-size distribution evolution of a compacted loess during consolidation and shearing. *J Soil Sediment* 20:2855–2867. <https://doi.org/10.1007/s11368-020-02621-3>
- Liu Y, Cao GZ, Meng YG, Liu MX (2013) Study on the microstructure feature and strength mechanism of the Tien Lake peat soil. *Adv Mater Res* 864–867:2695–2702. <https://doi.org/10.4028/www.scientific.net/AMR.864-867.2695>
- Lu N, Likos WJ (2006) Suction stress characteristic curve for unsaturated soil. *J Geotech Geoenviron* 132:131–142. [https://doi.org/10.1061/\(ASCE\)1090-0241\(2006\)132:2\(131\)](https://doi.org/10.1061/(ASCE)1090-0241(2006)132:2(131))
- Ma J et al (2021) Experimental study on vibration reduction technology of hole-by-hole presplitting blasting. *Geofluids* 2021:5403969. <https://doi.org/10.1155/2021/5403969>
- Mijares RG, Khire MV (2010) Soil water characteristic curves of compacted clay subjected to multiple wetting and drying cycles. *GeoFlorida*, pp 400–409. [https://doi.org/10.1061/41095\(365\)37](https://doi.org/10.1061/41095(365)37)
- Mu H, Deng Y, Li J (2018) Experimental study on strength characteristics of loess at ground fissures in Xi'an under action of dry and wet cycle. *J Eng Geol* 26:1131–1138. <https://doi.org/10.13544/j.cnki.jeg.2018022>
- Mu Q, Dong H, Liao H, Dang Y, Zhou C (2020) Water-retention curves of loess under wetting–drying cycles. *Géotechn Lett* 10:1–6. <https://doi.org/10.1680/jgele.19.00025>
- Muñoz-Castelblanco J, Pereira J, Delage P, Cui Y (2012) The water retention properties of a natural unsaturated loess from northern France. *Géotechnique* 62:95–106. <https://doi.org/10.1680/geot.9.P.084>
- Ng CWW, Sadeghi H, Hossen SKB, Chiu CF, Alonso EE, Baghbanrezvan S (2016) Water retention and volumetric characteristics of intact and re-compacted loess. *Can Geotech J* 53:1258–1269. <https://doi.org/10.1139/cgj-2015-0364>
- Ni W, Yuan K, Lü X, Yuan Z (2020) Comparison and quantitative analysis of microstructure parameters between original loess and remoulded loess under different wetting–drying cycles. *Sci Rep* 10:5547. <https://doi.org/10.1038/s41598-020-62571-1>
- Pan Z, Yang G, Ye W, Tian J, Liang B (2020) Study on mechanical properties and microscopic damage of undisturbed loess under dry and wet cycles. *J Eng Geol* 28:1186–1192. <https://doi.org/10.13544/j.cnki.jeg.2019-423>
- Peng J et al (2019) Distribution and genetic types of loess landslides in China. *J Asian Earth Sci* 170:329–350. <https://doi.org/10.1016/j.jseaes.2018.11.015>
- Phadnis HS, Santamarina JC (2011) Bacteria in sediments: pore size effects. *Géotechn Lett* 1:91–93. <https://doi.org/10.1680/geolett.11.00008>
- Romero E, Vecchia GD, Jommi C (2011) An insight into the water retention properties of compacted clayey soils. *Géotechnique* 61:313–328. <https://doi.org/10.1680/geot.2011.61.4.313>
- Sasanian S, Newson TA (2013) Use of mercury intrusion porosimetry for microstructural investigation of reconstituted clays at high water contents. *Eng Geol* 158:15–22. <https://doi.org/10.1016/j.enggeo.2013.03.002>
- Shao X, Zhang H, Tan Y (2018) Collapse behavior and microstructural alteration of remolded loess under graded wetting tests. *Eng Geol* 233:11–22. <https://doi.org/10.1016/j.enggeo.2017.11.025>
- Srland GH, Djurhuus K, Widere HC, Lien JR, Skauge A (2007) Absolute pore size distributions from NMR. *Diffus Fundam* 5(5):1–15
- Tang CS, Shi B, Wang BJ (2008) Factors affecting analysis of soil microstructure using SEM. *Chin J Geotech Eng* 30(4):560–565 (In Chinese)
- Tian H, Wei C (2014) A NMR-based testing and analysis of adsorbed water content. *Sci Sin Tech* 44:295–305. <https://doi.org/10.1360/092013-1133>
- Tian H, Wei C, Wei H, Yan R, Chen P (2014) An NMR-based analysis of soil-water characteristics. *Appl Magn Reson* 45:49–61. <https://doi.org/10.1007/s00723-013-0496-0>
- van Genuchten MT (1980) A closed-form equation for predicting the hydraulic conductivity of unsaturated soils. *Soil Sci Soc Am J* 44:892–898. <https://doi.org/10.2136/sssaj1980.03615995004400050002x>
- Vanapalli SK, Fredlund DG, Pufahl DE (1999) The influence of soil structure and stress history on the soil-water characteristics of a compacted till. *Géotechnique* 49:143–159. <https://doi.org/10.1680/geot.1999.49.2.143>
- Wang J, Li P, Ma Y, Vanapalli SK (2019) Evolution of pore-size distribution of intact loess and remolded loess due to consolidation. *J Soil Sediment* 19:1226–1238. <https://doi.org/10.1007/s11368-018-2136-7>
- Wang J, Zuo T, Li X, Tao Z, Ma J, Lian H (2021) Study on the fractal characteristics of the pomegranate biotite schist under impact loading. *Geofluids* 2021:1570160. <https://doi.org/10.1155/2021/1570160>
- Wei Y-n, Fan W, Yu B, Deng L-s, Wei T (2020) Characterization and evolution of three-dimensional microstructure of Malan loess. *CATENA* 192:104585. <https://doi.org/10.1016/j.catena.2020.104585>
- Xu J, Li Y, Ren C, Lan W (2020a) Damage of saline intact loess after dry-wet and its interpretation based on SEM and NMR. *Soils Found* 60:911–928. <https://doi.org/10.1016/j.sandf.2020.06.006>
- Xu J, Li Y, Wang S et al (2020b) Shear strength and mesoscopic character of undisturbed loess with sodium sulfate after dry-wet cycling. *Bull Eng Geol Environ* 79:1523–1541. <https://doi.org/10.1007/s10064-019-01646-4>
- Yao Y, Liu D (2012) Comparison of low-field NMR and mercury intrusion porosimetry in characterizing pore size distributions of coals. *Fuel* 95:152–158. <https://doi.org/10.1016/j.fuel.2011.12.039>
- Ye W, Bai Y, Cui C, Duan X (2020) Deterioration of the internal structure of loess under dry-wet cycles. *Adv Civ Eng* 2020:8881423. <https://doi.org/10.1155/2020/8881423>
- Yuan K, Ni W, Lü X, Vecchia GD, Wang H, Li L, Nie Y (2022a) Influence of wetting–drying cycles on the compression behavior of a compacted loess from microstructure analysis. *Bull Eng Geol Env* 81:348. <https://doi.org/10.1007/s10064-022-02854-1>
- Yuan K, Ni W, Lü X et al (2022b) Mechanical properties and microstructure evolution of Malan loess. *Quatern Int* 637:74–84. <https://doi.org/10.1016/j.quaint.2022.06.008>
- Zeng ZT, Lu HB, Zhao YL (2012) Wetting-drying effect of expansive soils and its influence on slope stability. *Appl Mech Mater* 170–173:889–893. <https://doi.org/10.4028/www.scientific.net/AMM.170-173.889>
- Zhang F, Yan B, Feng X, Lan H, Kang C, Lin X, Zhu X, Ma W (2019a) A rapid loess mudflow triggered by the check dam failure in a bulldoze mountain area, Lanzhou, China. *Landslides* 16:1981–1992. <https://doi.org/10.1007/s10346-019-01219-2>
- Zhang W, Sun Y, Chen W, Song Y, Zhang J (2019) Collapsibility, composition, and microfabric of the coastal zone loess around the Bohai Sea, China. *Eng Geol* 257:105142. <https://doi.org/10.1016/j.enggeo.2019.05.019>
- Zhao TY, Wang JF (2012) Soil-water characteristic curve for unsaturated loess soil considering density and wetting-drying cycle effects. *J Cent South Univ* 43(6):2445–2453 (In Chinese)

Zhu J, Han S, Zhang H (2022) Compression behavior and structure of undisturbed Q2 loess under wet-dry cycles. *Soils Found* 62:101165. <https://doi.org/10.1016/j.sandf.2022.101165>

author(s) or other rightsholder(s); author self-archiving of the accepted manuscript version of this article is solely governed by the terms of such publishing agreement and applicable law.

Springer Nature or its licensor (e.g. a society or other partner) holds exclusive rights to this article under a publishing agreement with the